LASER & PHOTONICS REVIEWS
www.lpr-journal.org

Vectorial Wavefront Manipulations Based on Misalignment Resilient Cascaded Metasurfaces

*Shifei Zhang, Peijin Li, Xue Zhang, Qunshuo Wei, Xin Li, Bo Wang, Junjie Li, Yongtian Wang, and Lingling Huang**

Due to spatial symmetry constraints, existing single-layer metasurface schemes suffer from reduced parallel control capabilities and information capacity in their Jones matrices. Recently, bilayer metasurface strategies have enabled significant enhancements in polarization and nonreciprocal modulations, facilitating applications in holographic display and optical communications. However, a more intuitive Jones matrix analysis is needed, and the current pixel-wise design of bilayer metasurfaces necessitates precise nanofabrication and alignment, leading to increased costs and technical challenges. In this paper, cascade metasurfaces design strategies for vectorial wavefront manipulations with misalignment robustness are investigated. First, an intuitive visualization method for the Jones matrix is established, based on the analysis of polarization eigenstates, polarization dichroism, and phase modulations. On this basis, a pixel-wise design approach of cascaded metasurfaces aimed at sophisticated vectorial spatial light modulation is proposed. This approach achieves assembly tolerances more than one order of magnitude higher than those of the control group, by employing a specialized spatial frequency optimization. Specifically, both the cascaded and individual metasurfaces are predesigned to serve distinct functions. Multichannel vectorial wavefront multiplexing and polarization encryption are all realized. It is believed that the work offers valuable insights into sophisticated polarization modulation techniques and the cost-effective design of multilayer metasurfaces.

1. Introduction

In recent years, metasurface-based optical signal modulation has emerged as a pivotal technology, driving breakthroughs in high-capacity and high-speed optical display,[1] communication,[2] detection,[3] imaging,[4] and computing.[5] This technology unprecedentedly leverages the multidimensional nature of optical information and its rich interactions with various physical fields. As the core optical element, the metasurface has redefined the optical platform, renowned for its compactness, design flexibility, and compatibility with semiconductor manufacturing processes. By skillfully designing their compositions, geometries, arrays, and other features, metasurfaces are capable of simultaneously modulating multiple optical variables, encompassing amplitude,[1d,6] phase,[1a,b] polarization,[1c,7] wavelength,[1b,8] and optical angular momentum.[1d,9]

Among versatile modulations, polarization modulation, and multiplexing have received significant research attention owing to their extensive applications in information multiplexing and optical detection. With a deepen comprehension of underlying mechanisms and enrichment of metasurface design strategies, the generation of arbitrary polarization states and various customizable anisotropic elements becomes feasible. As shown in **Figure 1**a, we define dichroism and retardance space to fully visualize the polarization modulation capabilities of various design strategies. The vector distributions follow the direction of the polarization eigenstates of metasurfaces, with norms associated with dichroism and retardance, respectively. As an illustrative example, the nanofin structure, commonly employed in metasurface designs, has polarization eigenstates that are determined by the axes of its geometric cross-section. By adjusting its geometric sizes, polarization dichroism, and retardance based on eigenstates become customizable. The polarization eigenstates can be extended to arbitrary linear polarization states through planar rotations.[10] Moreover, by integrating multiple independent units into a superpixel, it is possible to design unconstrained polarization eigenstates, as well as to develop full-Stokes polarizers[1c,11] and various waveplates.[1c,12] In some frameworks, each eigenstate can

S. Zhang, P. Li, X. Zhang, Q. Wei, X. Li, Y. Wang, L. Huang
Beijing Engineering Research Center of Mixed Reality and Advanced Display
School of Optics and Photonics
Beijing Institute of Technology
Beijing 100081, China
E-mail: huanglingling@bit.edu.cn

X. Zhang
Institute of Photonic Chips
University of Shanghai for Science and Technology
Shanghai 200093, China

B. Wang, J. Li
Beijing National Laboratory for Condensed Matter Physics
Institute of Physics
Chinese Academy of Sciences
Beijing 100190, China

The ORCID identification number(s) for the author(s) of this article can be found under https://doi.org/10.1002/lpor.202500309

DOI: 10.1002/lpor.202500309

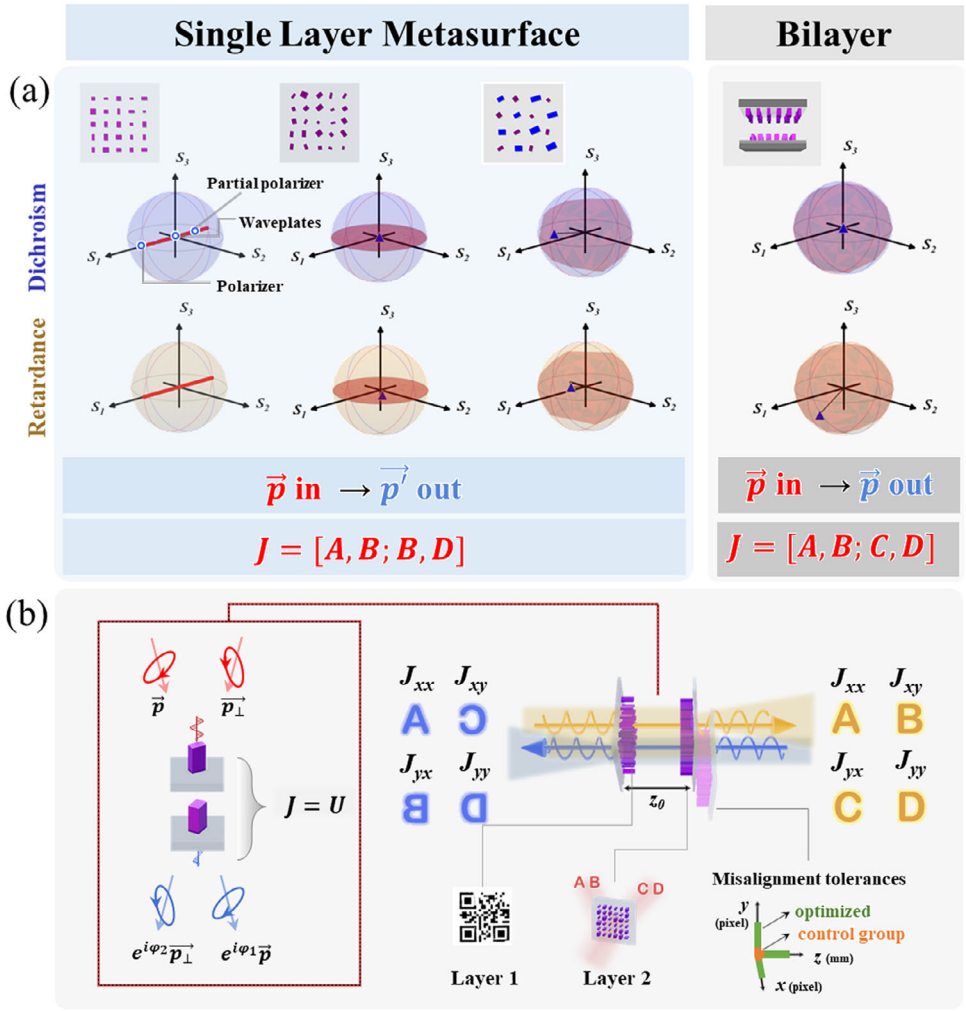

Figure 1. Advancements in Metasurface Design for Polarization Modulation and Schematic Overview of Our Study. a) The modulations of polarization eigenstates, polarization dichroism, and retardance progress with various single and double-layer metasurface designs. The directions of the dichroism and retardance vectors align with the polarization eigenstates, with their magnitudes indicating the respective dichroism and retardance values. The shaded regions illustrate the accessible ranges for the reconstructed dichroism and retardance vectors, with the blue triangle representing a specific instance within the shaded area. b) The principle of the cascaded metasurface design for vectorial wavefront multiplexing with misalignment robustness. Cascaded units with unitary Jones matrices are employed, with both individual layers and the cascaded metasurfaces being pre-designed for specific functionalities. The misalignment tolerances of these designs significantly exceed those of the control group.

be designed to possess an independent and tunable complex amplitude response.[13] Arranging meta-atoms with distinct polarization, phase, and even amplitude responses according to specific encoding rules enables spatially non-uniform and distinctive optical field controls, such as higher-order Poincaré sphere beams,[14] dynamic holographic display and encryption,[15] and optical vortex knots,[16] etc. Those capabilities promote metasurfaces as suitable substitutes for complex and bulky optical systems, which still require cascading multiple polarization and phase modulation components.

However, conventional single-layer metasurfaces are constrained by spatial symmetry, preventing them from breaking the restriction of identical off-diagonal elements in the Jones matrix.[1c,10b] Therefore, the Jones matrix permits only three independent channels,[14b,15d] resulting in a reduction of parallel control capabilities and information capacity. Moreover, the constructed full-Stokes polarizers and waveplates often demonstrate outgoing polarization states that are conjugate to the incident polarization states.[1c,11–13] To achieve comprehensive polarization modulations, it is necessary to develop improved metasurface design strategies to break the structural symmetry along the propagation direction.[10c,17] Recently, bilayer strategies have been employed to demonstrate observation of full-parameter Jones matrix,[17e] complete linear control of coherent light transmission,[17] and nonseparable polarization wavefront transformation.[10c] Undoubtedly, these bilayer metasurfaces significantly increase degrees of design freedom (DoFs). Through intelligent optimization algorithms and ingenious structural design, flexible polarization control capabilities are exhibited. Additionally, by integrating with modulations across various dimensions, bilayer metasurfaces expand the scope of potential applications, including non-reciprocal asymmetric polarization

encryption[18] and multiwavelength waveplates.[19] Nevertheless, a more intuitive Jones matrix analysis is needed to provide a more universal theoretical foundation for the expansion of information capacity across different applications. Additionally, challenges in the fabrication or opto-mechanical assembly of bilayer metasurfaces inevitably arise, particularly in meeting mass production requirements and achieving high-precision alignment. In this case, utilizing cascaded metasurfaces[20] allows for the independent fabrication of each constituent layer, thereby eliminating the need for alignment and overlay processes in manufacturing. By employing nanoimprint techniques or deep UV lithography, the manufacturing is further streamlined efficiently. Despite these manufacturing conveniences, the precision of metasurface assembly in previous works has uniformly adhered to pixel-level standards,[20b–f] increasing assembly costs, and raising concerns about the stability of the optical modules.

In this paper, we fully explore the design strategies of the anisotropic cascaded metasurface, aiming to enhance the modulation capability of vectorial wavefronts and improve assembly tolerances simultaneously. As shown in Figure 1b, starting from the modeling of cascaded units, we first demonstrate that the Jones matrix of bilayer metasurfaces can be designed as an arbitrary unitary matrix, both mathematically and computationally. Such enhanced polarization manipulation capabilities overcome the reciprocity constraints of the Jones matrix and facilitate independent wavefront modulations across diverse channels of the Jones matrix. Afterward, based on the significantly enhanced polarization modulation capability, we designed a pixel-wise design strategy for multichannel manipulations of vectorial wavefronts. This approach effectively exploits the inherent separability of cascaded metasurfaces and assigns distinct functionalities to the cascaded and separated metasurfaces in a deliberate and strategic manner. Through an optimized encoding principle, nine distinct holographic images arising from 4 independent Jones matrix channels are successfully constructed in the experiment, demonstrating a superior multiplexing capability and the high signal-to-noise ratios (SNR) of reconstructed signals. Concurrently, the first and second layers are respectively endowed with polarization encryption and holographic wavefront shaping functionalities. To improve the assembly tolerances of pixel-wise frameworks, a spatial frequency optimization is performed on the information encoding process of the first layer. While the cascaded sampling period and resolution remain unaffected, thereby ensuring superior display and modulation performance of metasurfaces. For comparison, we design a phase-cascaded metasurface without spatial frequency optimization to realize the Jones matrix holography. As validated, the optimized sample exhibits assembly tolerances of more than one order of magnitude higher than the control sample. Due to the robustness against axial displacements, although the cascaded metasurfaces are preset with an interlayer spacing of 100 μm, the optimized sample still manifests bidirectional modulations of vectorial wavefronts. We believe that our research not only presents a more promising and versatile platform for vectorial wavefront manipulation but also is valuable for the design of intelligent and compact optical modules leveraging multi-layer metasurfaces.

2. Principles and Methods

2.1. The Definition of Dichroism, Retardance, and Co-Phase Space

In this section, we utilize the Pauli vector and Stokes vector analysis method to parametrize the Jones matrix and polarization eigenstates of metasurfaces. We introduce the analyses of dichroism, retardance, and co-phase space to illustrate the enhanced capabilities of bilayer frameworks. Considering an anisotropic unit with orthogonal polarization eigenstates $\vec{p}$ and $\overrightarrow{p_\perp}$ (each is represented as a Stokes vector, and $\overrightarrow{p_\perp} = -\vec{p}$, both lying on the surface of the Poincaré sphere), and associated eigenvalues $t_1 e^{i\varphi_1}$ and $t_2 e^{i\varphi_2}$ (where t_1 and t_2 represent the amplitude response, $e^{i\varphi_1}$ and $e^{i\varphi_2}$ denote the phase response), the birefringent transmitted property can be parametrized by using the exponential of Pauli vector as:[21]

$$J = \exp\left(\frac{\alpha_0 - i\beta_0}{2}\right)\exp\left(\frac{\alpha - i\beta}{2}\vec{p}\vec{\sigma}\right) \tag{1}$$

where $\alpha_0 = \ln(t_1 t_2)$, $\alpha = \ln t_1 - \ln t_2$, $\beta_0 = -(\varphi_1 + \varphi_2)$, $\beta = \varphi_2 - \varphi_1$, it can be seen that α and β are respectively related to polarization dichroism and retardance, while β_0 indicates a common phase (co-phase) response. Furthermore, we defined the dichroism vector $\vec{D}$, retardance vector $\vec{R}$, and co-phase vector $\vec{C}$ by incorporating $\vec{p}$, as detailed below:

$$\begin{aligned} \vec{D} &= |\tanh\alpha|\,\vec{p} && \alpha \in (-\infty, +\infty) \\ \vec{R} &= \frac{1}{2}\left[\sin\left(\frac{\beta}{2}\right) + 1\right]\vec{p} && \beta \in [-\pi, +\pi] \\ \vec{C} &= \frac{1}{2}\left[\sin\left(\frac{\beta_0}{2}\right) + 1\right]\vec{p} && \beta_0 \in [-\pi, +\pi] \end{aligned} \tag{2}$$

within the definition, all vectors are oriented congruently with the Stokes vector $\vec{p}$, and their magnitudes are confined within the range from 0 to 1. This enables the representation of these distributions within unit spheres that are referenced to the coordinate systems (s_1, s_2, s_3), facilitating the visualization of dichroism, retardance, co-phase, and polarization eigenstates simultaneously. As shown in Figure 1a, with the escalation of design complexity, polarization modulation becomes more comprehensive, enabling the expansion of polarization eigenstates to arbitrary orientations (More details are provided in Section S1, Supporting Information). Particularly, by using a metasurface with bilayer frameworks, full-Stokes polarizers, as well as various waveplates can be designed. Correspondingly, the dichroism and retardance spaces are totally covered, where the dichroism vectors distributed on the unit spherical surface are related to polarizers, and the dichroism vectors at the spherical center represent waveplates.

2.2. Design Strategy for Cascaded Units

In this context, we start from the unit design of cascaded metasurfaces and demonstrate its superior capacity in lossless

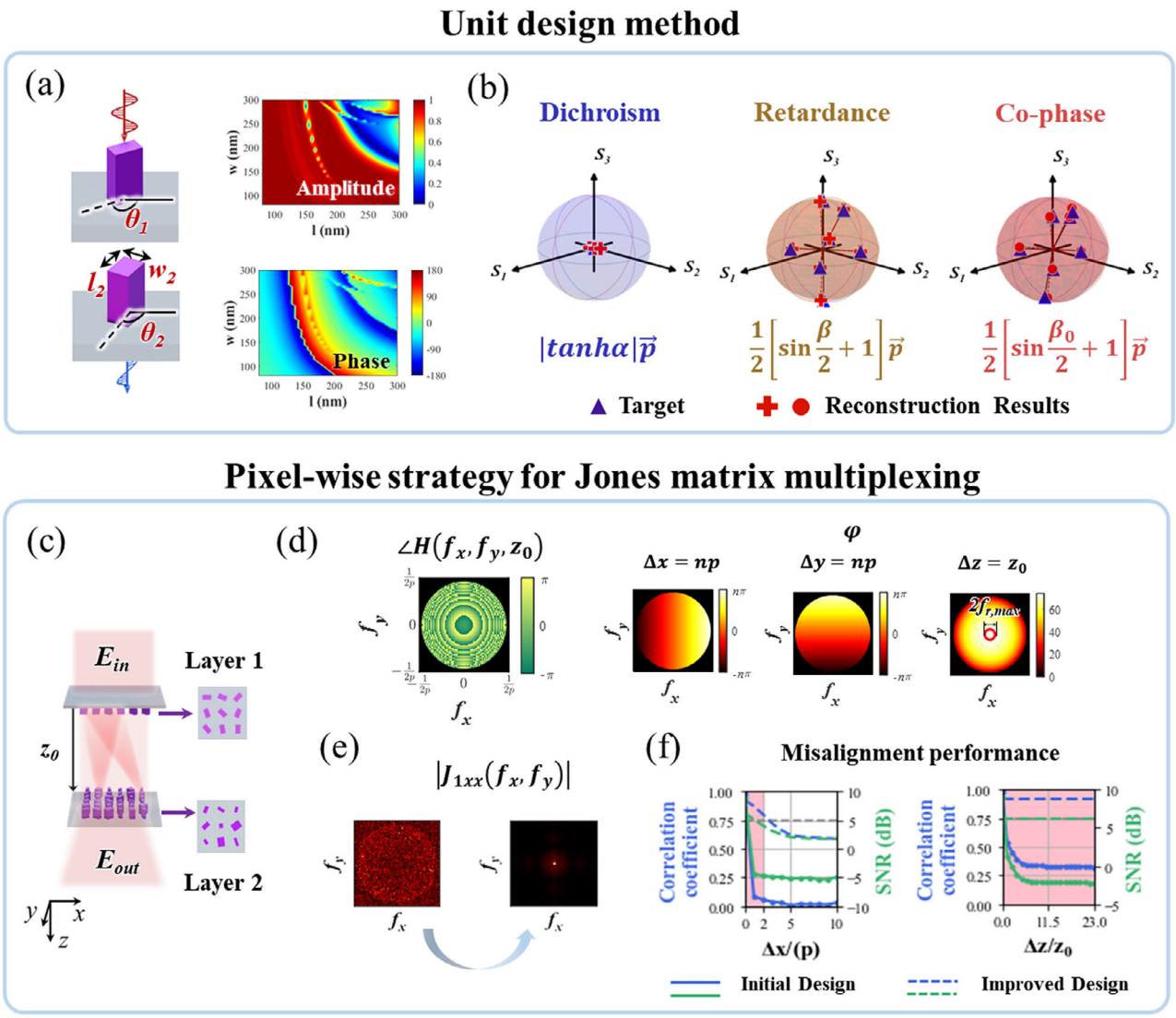

Figure 2. Cascaded unit design and pixel-wise design for polarization modulation. a) Structural diagram and optical response of the cascaded units, designed by leveraging four DoFs, comprising two rotation angles and the dimensions of nanofins in length and width. b) The polarization modulation properties, visualized within the dichroism, retardance, and co-phase space, based on the established structure library. The blue and red markers denote the target and reconstructed vectors, respectively, showcasing a high degree of consistency. c) Schematic representation of a pixel-wise cascaded metasurface with a predefined interlayer spacing, denoted as z_0. d) Distribution of the AS transfer function and the induced phase under 3D misalignment, presented in the spatial frequency domain. e) Optimization of the spatial frequency for the first layer, demonstrating the transition from the initial design to an improved version. f) Misalignment assessment of initial design and improved design in terms of holographic reconstruction performance.

birefringent polarization modulation mathematically and algorithmically. By applying such a design strategy, cascaded units characterized by arbitrary unitary Jones matrix are available. Namely, the cascaded units possess arbitrary polarization eigenstates, and for each eigenstate, they exhibit a tunable and independent phase response. In this instance, α_0 and dichroism α equal zero, and $\vec{D}$ is in the origin of dichroism space. Given the need for flexible adjustment of $\vec{p}$, β, and β_0, the metasurface design necessitates a minimum of 4 DoFs for structural parameters. Our employed scheme is shown in **Figure** 2a, the cascaded units are made of amorphous silicon (α-Si) nanofins. The first layer functions as a half-wave plate with a tunable planar rotation angle (θ_1), and the second layer operates as a lossless waveplate with adjustable length (l_2), width (w_2), and planar rotation angle (θ_2). The working wavelength is set at 875 nm, and the meta-atoms period and height are configured to 400 and 600 nm, respectively. Utilizing the finite element method, we conduct a parameterized sweep of the optical response for nanofins with varying lengths and widths. The optical responses along the fast axis are depicted in Figure 2a. Given the geometric interchangeability of the nanofins' length and width, the optical responses along the short axis exhibit a transposed symmetry. Based on the simulation results, a nanofin with approximately uniform energy conversion and half-wave phase delay is selected as the unit of the first layer. Additionally, a structure library with tunable phases and amplitude is established for the design of the second layer. By manipulating combinations of structural parameters ($\theta_1, \theta_2, l_2, w_2$), we calculate the ranges of cascaded

polarization eigenstates, retardance, and co-phase values. Following the laboratory coordinate system, each layer has an independent common phase β_{0n} and retardance β_n, as well as a linear polarization eigenstate $\overrightarrow{p_n}$, which n represents the layer index. For the first layer, the retardance value $\beta_1 = \pi$. While for the second layer, both retardance and common phase are adjustable based on the established structure library. The Jones matrix of the cascaded metasurface is formulated as indicated below:

$$
\begin{aligned}
J &= J_2 J_1 = \prod_{n=1}^{2} e^{-\frac{i\beta_{0n}}{2}} e^{-\frac{i\beta_n}{2}\overrightarrow{p_n}\overrightarrow{\sigma}} = e^{-\frac{i\beta_0}{2}} e^{i\frac{\beta}{2}(\vec{p}\vec{\sigma})} \\
\cos\frac{\beta}{2} &= -\overrightarrow{p_2}\cdot\overrightarrow{p_1}\sin\frac{\beta_2}{2} \\
\vec{p} &= \frac{1}{\sin\frac{\beta}{2}}\left(\overrightarrow{p_1}\cos\frac{\beta_2}{2} - \overrightarrow{p_1}\times\overrightarrow{p_2}\sin\frac{\beta_2}{2}\right) \\
\beta_0 &= \beta_{01} + \beta_{02}
\end{aligned}
\tag{3}
$$

As can be seen, the cascaded retardance and polarization eigenstate β and $\vec{p}$ are determined by the linear polarization eigenstates $\overrightarrow{p_1}$ and $\overrightarrow{p_2}$ (which are related to the rotation angles θ_1 and θ_2), and the retardance values of the second layer β_2. Owing to the term of $\overrightarrow{p_1}\times\overrightarrow{p_2}$, the polarization eigenstate $\vec{p}$ is no longer confined to the S1-S2 plane within the Poincaré sphere, but can be designed with more possibilities. This can encompass the entirety of polarization states, and break the limitation of previous constraints that input and output polarizations must remain conjugate. While the common phase β_0 can be also flexibly designed by adjusting β_{02}. Through extensive sampling of random combinations $(\overrightarrow{p_1}, \overrightarrow{p_2}, \beta_2, \beta_{02})$ and calculation based on Equation (3), we obtain the ranges of eigenstate, dichroism, retardance, and common phase. The results are translated into dichroism vector set $\{\overrightarrow{D}\}$, retardance vector set $\{\overrightarrow{R}\}$, and co-phase vector set $\{\overrightarrow{C}\}$, and mapped to the shaded regions in Figure 2b. As can be seen, the shaded area of the dichroism vector set collapses near the origin, demonstrating a lossless modulation. The range of retardance and co-phase vectors covers the entire space.

To further clarify the feasibility of designing arbitrary $\vec{p}$ and β, we initiate an inverse calculation process to derive possible structural parameters from given target polarization modulations. We randomly preset various combinations of $(\vec{p}, \beta)$ (which $\{\vec{p}\}$ include circular, linear, and elliptical polarizations), and utilize an optimization algorithm to calculate the possible parameter combinations $(\overrightarrow{p_1}, \overrightarrow{p_2}, \beta_2)$ and $(\theta_1, \theta_2, l_2, w_2)$ for each scenario. The reconstructed polarization eigenstates $\{\overrightarrow{p'}\}$ exhibit only minor differences compared to targets. The mean Euclidean distance of $\{\overrightarrow{p'}\}$ and $\{\vec{p}\}$ in the Poincaré sphere (defined as $\|\overrightarrow{p'} - \vec{p}\|$)[11a] is ≈0.031. And the mean difference between the reconstructed values of dichroisms $\{\tan|\alpha'|\}$ and retardances $\{\beta'\}$, and their respective target values are 0.017° and 1.54°, respectively. The vectors $\{\overrightarrow{D}\}$ and $\{\overrightarrow{R}\}$ associated with a target $\{\vec{p}\}$, $\{\tan|\alpha|\}$ and $\{\beta\}$ are presented as blue triangles in Figure 2b. And the corresponding reconstructed results of $\{\overrightarrow{D'}\}$ and $\{\overrightarrow{R'}\}$ are depicted as red crosses, which have shown high fidelity with the target blue triangles (More details are provided in Section S2, Supporting Information).

Furthermore, by performing a similar analysis as before, it is possible to customize the new common phase β_0 simultaneously. The mean difference between the optimal reconstructions and the target values is 3.02°. As depicted, the close overlap of target vectors $\{\overrightarrow{C}\}$ and reconstruction vectors $\{\overrightarrow{C'}\}$ evinces the flexible phase control of β_0.

To conclude, based on the structural parameter design of cascaded units, arbitrary polarization eigenstates, as well as dual independent and tunable phases are available. This endows the Jones matrix with any unitary matrix possibilities theoretically. According to Equation (3), the expansion of the scope of polarization eigenstates allows the off-diagonal elements of the Jones matrix to break the reciprocity restriction. This provides foundations for independent wavefront modulations across various channels of the Jones matrix through a pixel-wise design of cascaded metasurfaces.

2.3. Design Strategy of Pixel-Wise Cascaded Metasurfaces for Multichannel Vectorial Manipulation

As mentioned above, by configuring J_{xx}, J_{xy}, J_{yx} and J_{yy} the basic multiplexing channels, and employing the holographic technique, multichannel wavefront shaping functions in specific spaces can be designed, which will further increase the parallelism and versatility of anisotropic metasurfaces.

First, we establish a transmission model for pixel-wise cascaded metasurfaces. Considering practical opto-mechanical assembly and evaluation for axial displacements, we reserve a certain interval z_0 between layers. In this instance, each pixel of the first layer, which contributes modulations of the Jones matrix $J_1(x, y)$, can be envisioned as an anisotropic Huygens point source under the coherent light incidence. According to the angular spectrum (AS) method, the output of the first layer can also be characterized by a superposition of coherent waves with diverse spatial frequencies, represented as $J_1(f_x, f_y)$ in the spatial frequency domain. As the secondary waves propagate over a preset distance z_0, these contribute an input $J_{2,in}(x, y, z_0)$ to the second layer, which can be denoted by $J_{2,in}(x, y, z_0) = \mathfrak{F}^{-1}\{H(f_x, f_y, z_0)J_1(f_x, f_y)\}$. $H(f_x, f_y, z_0)$ represents the angular spectrum transfer function of the spatial frequency domain (f_x, f_y) with a propagation distance z_0, defined as $\exp(i2\pi\sqrt{\frac{1}{\lambda^2} - f_x^2 - f_y^2}z_0)$ ($2\pi\sqrt{\frac{1}{\lambda^2} - f_x^2 - f_y^2}$ is also referred to as transverse wave vector k_z), and $\mathfrak{F}$ represents the Fourier transform operator. As shown in Figure 2d, $H(f_x, f_y)$ acts as a low-pass filter during propagation, with a region of spatial frequencies above the threshold of $\frac{1}{\lambda}$ (shaded in black) where the wave is evanescent. Subsequently, the units of the second layer $J_2(x, y)$ interacts with the input field $J_{2,in}(x, y, z_0)$ pixel by pixel and outputs the final cascaded result $J(x, y)$. That is, $J(x, y) = J_2(x, y)J_{2,in}(x, y, z_0)$. To demonstrate the independent modulations across the channels of $J(x, y)$, we encode four distinct far-field holographic images E_{fxx}, E_{fxy}, E_{fyx}, and E_{fyy} into J_{xx}, J_{xy}, J_{yx} and J_{yy}, respectively. By establishing an analytical iteration retrieval, the distribution of $J(x, y)$, as well as structural parameters $[\theta_1(x, y), \theta_2(x, y), l_2(x, y), w_2(x, y)]$, are obtained. The reconstructed results across four channels demonstrate high fidelity with the target holographic images, as evidenced by correlation

coefficients that exceed 0.97. However, this pixel-by-pixel scheme is sensitive to 3D misalignments. In the case of only one lateral pixel displacement and one wavelength axial displacement, the reconstructed light fields are filled with noise, and the average correlation coefficient rapidly drops below 0.1 and 0.7, respectively (The relative algorithm flowchart and simulation results are provided in Section S3, Supporting Information).

The high misalignment sensibility of the initial cascaded scheme attributes to the distortion of $J_{2,in}(x, y, z_0)$. According to the shifting properties of Fourier transform, displacements in the spatial domain induce phase shifts in the frequency domain, thereby the deformed input field $J'_{2,in}(x, y, z_0)$ with 3D misalignments Δx, Δy, and Δz can be derived as:

$$J'_{2,in}(x, y, z_0) = \mathfrak{F}^{-1}\left[e^{i\varphi(f_x,f_y)} H(f_x, f_y, z_0) J_1(f_x, f_y)\right]$$
$$\varphi(f_x, f_y) = 2\pi(f_x \Delta x + f_y \Delta y) + k_z \Delta z \quad (4)$$

As can be seen, the distortion depends on the additional phase modulation $\varphi(f_x, f_y)$ across the spatial frequency domain. The lateral displacements Δx and Δy introduce directional increments in the distribution of $\varphi(f_x, f_y)$ across the f_x and f_y directions, respectively. Whereas the axial displacement Δz induces a varied distribution of $\varphi(f_x, f_y)$ along the direction of radial frequency f_r (defined as $\sqrt{f_x^2 + f_y^2}$). (Figure 2d) Noteworthy, the key to the degree of distortion is related to the gradients of phase, that is, $\nabla\varphi(f_x, f_y)$, rather than the value of $\varphi(f_x, f_y)$ itself. That means, if $\varphi(f_x, f_y)$ is nearly consistent in the frequency domain, denoted as a a constant phase φ_c, then it can be extracted from the Fourier operator. And the deformed field $J'_{2,in}(x, y, z_0)$ becomes $e^{i\varphi_c} J_{2,in}(x, y, z_0)$, it will have little impact on the results of our pixel-wise framework. Although the axial misalignment leads to greater values of $\varphi(f_x, f_y)$ in low-frequency regions, the corresponding gradient $\nabla\varphi(f_x, f_y)$ is less pronounced. Therefore, the light field encoded in this range is more robust to misalignments theoretically. Additionally, as the phase gradients induced by lateral displacements maintain consistency, the key to enhancing robustness against such displacements is to set an appropriate frequency bandwidth. To conclude, confining the spatial frequency of the information encoded in the first layer to a low-frequency range with a defined bandwidth will enhance robustness against both lateral and axial misalignments. However, in the previous initial design, a considerable portion of the encoded fields of the first layer is distributed in the high-frequency range, especially in the region of evanescent waves (Figure 2e), thereby the output fields undergo significant mutations with displacements. It should be noted that, due to the unchanged sampling parameters in the second layer, the cascaded sampling rate and spatial frequency bandwidth remain consistent with the initial design, which ensures a larger NA and higher resolution for the modulated light field.

Subsequently, we demonstrate the feasibility of the spatial frequency optimization design and assess its performance under diverse misalignments. To exemplify, we restrict the available frequency domain by setting a threshold for $\Delta\varphi$. The well-defined bandwidth is determined according to the calculated results of the radial frequency $f_{r,\max}$ under $\Delta z = z_0$ and $\Delta\varphi = \frac{\pi}{4}$, which also contributes to the robustness against Δx and Δy. According to the maximum radial frequency $f_{r,\max}$, the sampling spacing D of the first layer can be determined (More details are provided in Section S4, Supporting Information). Afterward, 1000 patterns with the determined sampling spacing are randomly generated and assigned as the polarization encryption distributions of the first layer. By imposing polarization constraints to the first layer's distribution on prior algorithm iteration, high-quality holographic reconstructions across all four Jones channels are obtained in all instances, which demonstrates the universality of our scheme. The correlations between the reconstructed data and their respective targets exceed the threshold of 0.92. Lastly, we calculate the changes in mean correlation coefficients and mean signal-to-noise ratios (SNRs) across four channels in response to lateral and axial displacements. As observed in Figure 2f, the improved design, despite a minor reduction in peak SNR compared to the initial scheme, exhibits a significantly improved performance against misalignments. Especially for the axial displacements up to 23 times z_0, the performance remains remarkably consistent, indicating a substantially enhanced tolerance. For the lateral displacement, the mean correlation coefficients, and the mean SNR of reconstructed images across four channels remain above 0.75 and 4.0 for in-plane displacements within a range of ±2 pixel, respectively. The corresponding displacement tolerances can be determined by setting a correlation coefficient threshold, which typically ranges from 0.7 to 0.8,[15a,22] based on the requirements of given applications. The lateral displacement tolerances can be further improved by further designing the range of f_x and f_y simultaneously.

3. Experiments and Results

Based on the established structure library and spatial frequency optimization principle, we design a cascaded metasurface for vectorial wavefront multiplexing. In contrast to previously reported Jones matrix holography,[10c,17d,e,23] we design wavefront shaping functions for the cascaded metasurface and separable metasurfaces simultaneously. In addition, the cascaded framework exhibits significantly improved misalignment robustness, with maximum lateral and axial displacement tolerances of 20 times and 18 times higher than those of the control group that lack spatial frequency optimization. Furthermore, due to the improved axial misalignment tolerance, the cascaded framework with a non-ignorable interlayer spacing exhibits a bidirectional operational mode and nonreciprocal modulations in J_{xy} and J_{yx} channels.

3.1. Multichannel Vectorial Holography by using a Cascaded Metasurface with Spatial Frequency Optimization

In this design, the first layer acts as a polarization encryption element, arranged by half-wave plate meta-atoms. While the second layer undertakes anisotropic phase modulations. The polarization encrypted patterns of the first layer are designed as a binary Quick Response (QR) code, exhibiting complementary intensity distributions $|a_1(x, y)|^2$ and $|a_2(x, y)|^2$ in the diagonal and off-diagonal channels of $J_1(x, y)$, respectively. Correspondingly, the Jones matrix of the first layer can be denoted as $J(x, y) = a_1(x, y)\sigma_z + a_2(x, y)\sigma_x$, where σ_z and σ_x are

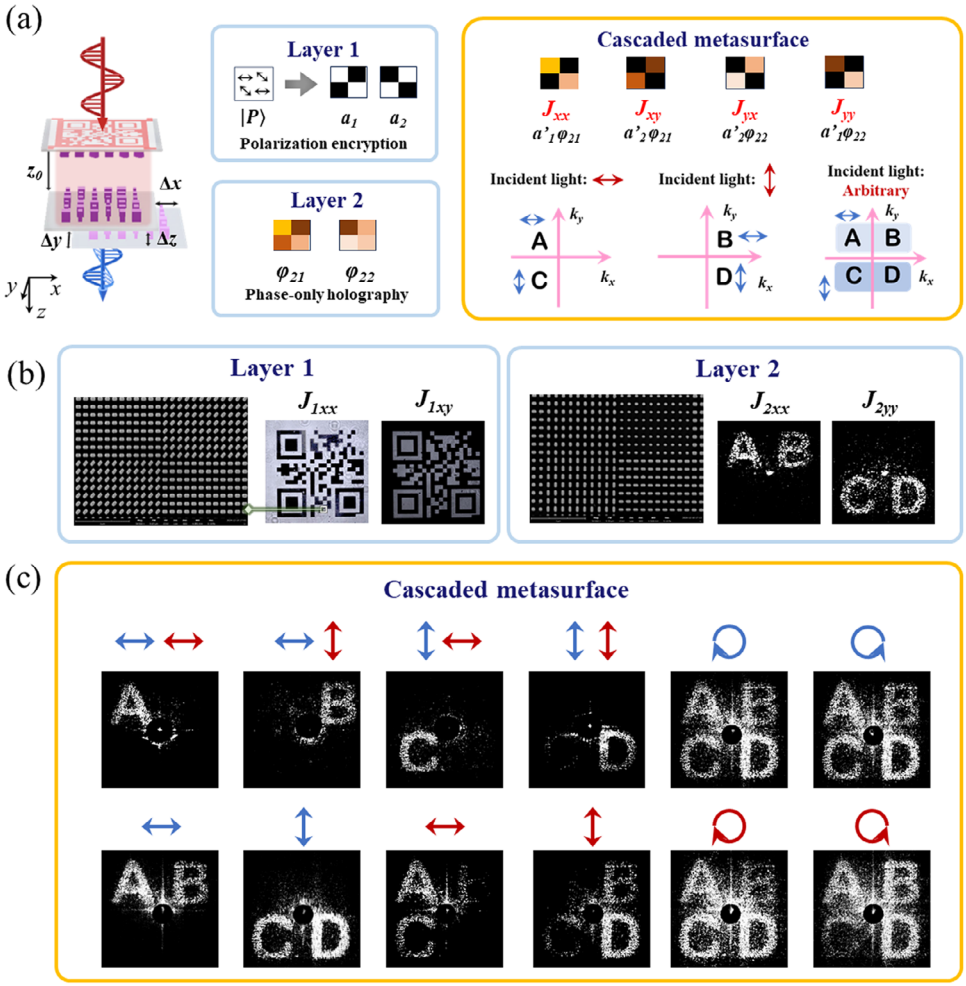

Figure 3. Design and experimental validation of pixel-wise cascaded metasurfaces for Jones matrix holography. a) The design scheme for each layer and the cascaded metasurface. The first layer is designed for polarization encryption with an optimized spatial frequency, while the second layer serves as a birefringent phase modulator. The cascaded metasurface integrates amplitude and phase information from both layers, enabling a variety of polarization multiplexing capabilities. b) SEM images and experimental results of Layer 1 and Layer 2, demonstrating the functions of polarization encryption and birefringent holography, respectively. c) Experimentally captured images of the cascaded metasurfaces across different polarization channels, showcasing the versatility of polarization manipulation.

Pauli matrices, and $a_2(x, y) = 1 - a_1(x, y)$. After propagation, the input light field to the second layer can be expressed as $J_{2,in}(x, y, z_0) = a'_1(x, y, z_0)\sigma_z + a'_2(x, y, z_0)\sigma_x$, where $a'_j(x, y, z_0)$ is the diffractive field of $a_j(x, y)$ $(j = 1, 2)$. To further simplify the optical encoding process, we only utilize the diagonal elements of $J_2(x, y)$ for phase modulations, defined as $J_{2xx}(x, y) = e^{i\varphi_{21}(x,y)}$ and $J_{2yy}(x, y) = e^{i\varphi_{22}(x,y)}$. With the pixel-by-pixel interaction of $J_2(x, y)$ and $J_{2,in}(x, y, z_0)$, the output light field of this cascaded framework can be derived as follows:

$$J(x, y) = \begin{bmatrix} a'_1(x, y)\, e^{i\varphi_{21}(x,y)} & a'_2(x, y)\, e^{i\varphi_{21}(x,y)} \\ a'_2(x, y)\, e^{i\varphi_{22}(x,y)} & -a'_1(x, y)\, e^{i\varphi_{22}(x,y)} \end{bmatrix} = \begin{bmatrix} h_A & h_B \\ h_C & h_D \end{bmatrix} \quad (5)$$

As can be seen, the cascaded elements are integrated with the diffractive fields of amplitude distributions a'_1 and a'_2, as well as the phase profiles, $e^{i\varphi_{21}}$ and $e^{i\varphi_{22}}$. The four complex-amplitude combinations, $a'_1 e^{i\varphi_{21}}$, $a'_2 e^{i\varphi_{21}}$, $a'_2 e^{i\varphi_{22}}$, and $a'_1 e^{i\varphi_{22}}$ can be utilized to respectively encode four unique holograms h_A, h_B, h_C, and h_D, which effectively extends the independent holographic multiplexing capacity of the Jones matrix to four channels. As shown in **Figure 3**, a'_1 and a'_2 primarily perform a filtering function, the holographic information is predominantly encoded by the phase components $e^{i\varphi_{21}(x,y)}$ and $e^{i\varphi_{22}(x,y)}$. Therefore, $e^{i\varphi_{21}(x,y)}$ records the holograms of cascaded channels J_{xx} and J_{xy} simultaneously, and $e^{i\varphi_{22}(x,y)}$ is encoded with those of channels J_{yx} and J_{yy} at the same time. Thereby, the anisotropic phase modulations of the second layer are manifested as hologram combiners of the cascaded channels. So far, both cascaded metasurfaces and separable metasurfaces are assigned with specific functions. The cascaded metasurfaces are designed for a four-channel independent vectorial holography, while single-layer metasurfaces are utilized for polarization encryption and dual-channel holography. Moreover, the scheme features high-SNR and high-fidelity reconstruction, thus offering more intriguing multiplexing possibilities across diverse input and output polarized

channels (More details can be found in Section S5, Supporting Information).

The metasurfaces are designed with a size of 500 μm, and the interlayer distance is set at 100 μm. To experimentally demonstrate the effect of pixel-level displacements, we utilize macro pixels with a size of 4 μm as encoded units. The spatial sampling spacing of the first layer, which corresponds to a maximum spatial frequency of 0.025 cycle μm^{-1}, is set as 20 μm to improve the misalignment tolerances. The maximum phase difference ($\Delta\varphi(f_x,f_y)$) introduced under displacements of $\Delta x_{\max} = \pm 2p_m$, $\Delta y_{\max} = \pm 2p_m$ and $\Delta z_{\max} = 10z_0$ are 0.8π, 0.8π and 1.06π, respectively, which p_m represents the size of macro pixels. Due to the separable design strategy, the cascaded metasurfaces can be fabricated based on a single-layer process without a precision overlay process. Here we used a standard laboratory micro/nano manufacturing process, which is mainly based on electron beam lithography (EBL) and reactive ion beam etching (RIE). The scanning electron microscopy (SEM) images of samples are provided in Figure 3b. Additionally, nanoimprinting (NIL) and deep ultraviolet (DUV) lithography can be applied to replace the EBL process, facilitating mass-production of such intelligent modules.

The optical setup consists of both a near-field observation and a far-field Fourier transform optical path, by using a polarization insensitive beam splitter (BS). The cascaded metasurface is placed on a precision stage with six degrees of freedom for adjustment. The adjustable accuracy of the alignment platform achieves 1 μm, to ensure the reliable detection of misalignment performance (More details are provided in Figure S13, Supporting Information).

First, we measure the independent functions of separable metasurfaces (Figure 3b). The near-field imaging of the first layer displays varying intensities across diverse polarization selections, revealing a complementary QR code distribution in channels J_{1xx} and J_{1xy}. And the second layer presented holographic letter combinations "A" + "B" and "C" + "D" in channels J_{2xx} and J_{2yy}, respectively. The holographic letters "A", "B", "C" and "D", positioned in distinct quadrants of momentum space, emerge in the Jones matrix channels J_{xx}, J_{xy}, J_{yx}, and J_{yy} respectively. By varying the polarization of input or output, a variety of reconstructed letter combinations can be expected. Since J_{xy} and J_{yx} breaks the symmetry restrictions, applying the same polarization selection solely to the incident or output space may lead to distinct modulation effects. For an arbitrary polarization state $|p\rangle = [\cos\chi, \sin\chi e^{i\psi}]^T$, the modulation effects in the incident and output spaces can be described as follows:

$$J_p^{in} = J|p\rangle = \left[h_A\cos\chi + h_B\sin\chi e^{i\psi}, h_C\cos\chi + h_D\sin\chi e^{i\psi}\right]^T$$
$$J_p^{out} = \langle p|J = \left[h_A\cos\chi + h_C\sin\chi e^{-i\psi}, h_B\cos\chi + h_D\sin\chi e^{-i\psi}\right] \quad (6)$$

As observed, J_p^{in} and J_p^{out} record the combinations of holograms h_A, h_B, h_C, and h_D with distinct coefficients, which are associated with the selected polarization state. According to Equation (6), we can obtain $J_x^{in} = [h_A, h_C]^T$, $J_x^{out} = [h_A, h_B]$, $J_y^{in} = [h_B, h_D]^T$, $J_y^{out} = [h_C, h_D]$, $J_{l(r)}^{in} = [h_A \pm ih_B, h_C \pm ih_D]^T$, $J_{l(r)}^{out} = [h_A \mp ih_C, h_B \mp ih_D]^T$. Among these polarization channels, J_r^{in}, and J_l^{in} are representatives of "arbitrary incident." In terms of the linear properties of the Fourier Transform, the far-field holographic reconstruction of each multiplexed channel also follows the combination rule with corresponding weight factors. As shown in Figure 3c, we measure the holographic reconstructions across 12 channels, successfully demonstrating 9 distinct modulations originating from 4 independent Jones matrix channels. The measured channels are: J_{xx}, J_{xy}, J_{yx}, J_{yy}, J_x^{out}, J_y^{out}, J_x^{in}, J_y^{in}, J_r^{out}, J_l^{out}, J_r^{in}, and J_l^{in}. And all combinations of holographic letters are: "A", "B", "C", "D", "A" + "B", "C" + "D", "A" + "C", "B" + "D", and "A" + "B" + "C" + "D", which are consistent with the results obtained from Equation (6). Due to the incomplete energy conversion, weak crosstalk of letters "B" and "C" can be observed in the channels J_x^{in} and J_y^{in} (More analysis is provided in Section S6, Supporting Information). The unconverted background light forms a zero spot on the observed far-field plane. To eliminate the zero spot and facilitate observation, we perform a high pass filter to the output momentum space by using a chromium mask. Compared with previous research in multichannel vectorial holography,[15d] the cascaded metasurfaces significantly enhanced the modulation possibilities, and the number of independent Jones matrix channels increased from 3 to 4, while the variety of distinct multiplexing channels expanded from 7 to 9, respectively. Note that, since the multiplexing channels are based on the combination of Jones matrix channels, noise from the Jones matrix channels accumulates in the multiplexed channels. This may lead to a decrease in the SNR of the holographic images in multiplexing channels.

3.2. The Demonstration of 3D Misalignment Robustness

Subsequently, we measure and analyze the 3D misalignment performance of cascaded metasurfaces, which are conducted separately for misalignments along the x, y, and z axes. The correlation coefficient between the reconstructed image and the respective target is employed as the assessment metric, and a correlation coefficient threshold of 0.7 is set to determine misalignment tolerances. The simulation and experimental results of correlation coefficients are plotted in **Figure 4b**. The results showcase two types of misalignment tolerance ranges, corresponding to the diagonal and off-diagonal channels of the cascaded Jones matrix. As observed, the misalignment tolerances of all channels notably surpass those of preceding studies (about a lateral displacement tolerance of ±1 macro pixel and an axial displacement tolerance of about +200 μm[20c–f]). For lateral displacement, the experimental results show strong agreement with the simulation results. Channels J_{xx} and J_{yy} maintain high coherence up to 20 macro pixels in both simulation and experiment. Similarly, channels J_{xy} and J_{yx} exhibit high-fidelity reconstruction within 2 macro pixels experimentally, the measured tolerances are slightly lower than those predicted by simulations. For axial displacement, although the experimental results show a decrease relative to the simulation results, the correlation coefficients of J_{xx}, J_{xy} and J_{yx} all surpass the preset threshold across a displacement range of −100–400 μm. Notably, the maximum displacement tolerance for the channel J_{xx} can reach up to 900 μm. For axial displacements exceeding 400 μm, partial crosstalk is introduced to channels J_{xy} and J_{yx}, but the holographic letters remain visually discernible (More details and raw image data are provided in Figures S16–S18, Supporting Information). The

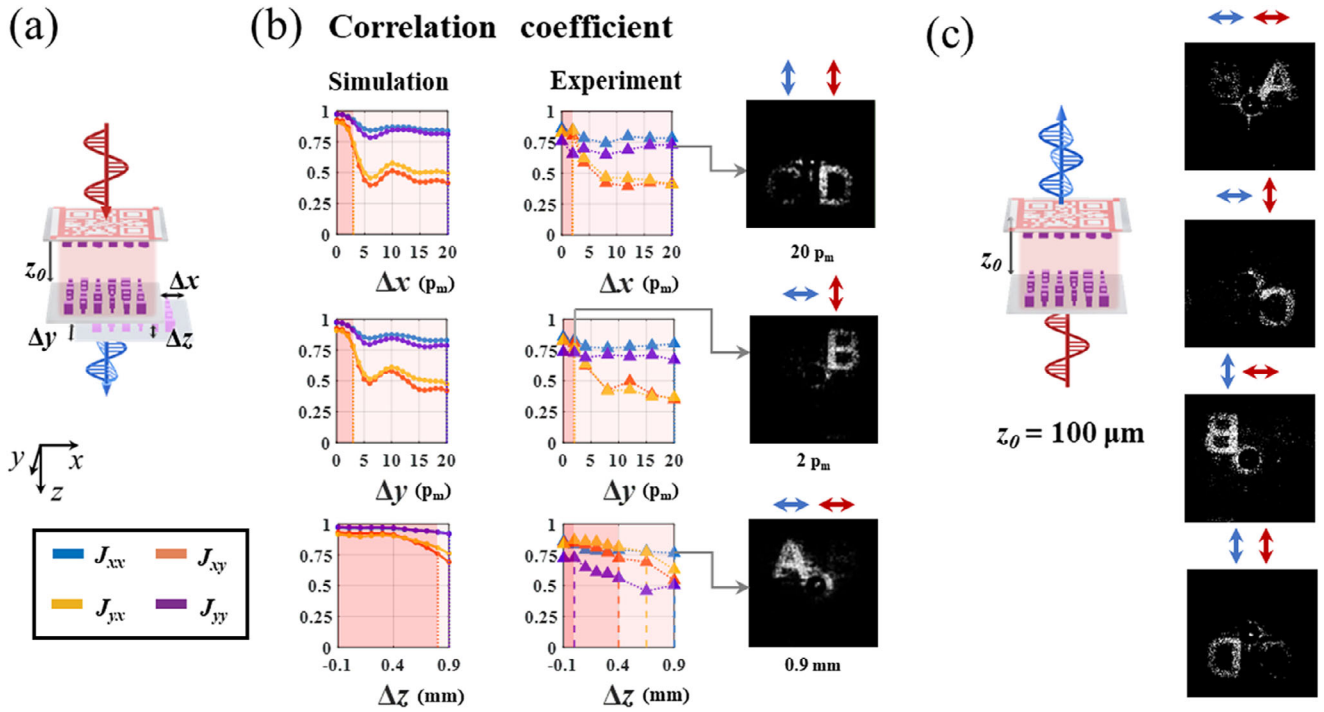

Figure 4. Design and experimental validation of pixel-wise cascaded metasurfaces for Jones matrix holography. a) Schematic representation of the cascaded metasurface with 3D misalignments. b) Misalignment assessment of the pixel-wise cascaded metasurfaces, determined by the correlation coefficient of holographic reconstructions, with both simulated and experimental results depicted. c) Experimental validation of backward vectorial wavefront manipulation based on the cascaded metasurfaces with a preset interlayer spacing.

undesired degradation observed in the channel J_{yy} is related to the inadequate modulation of $J_{1,yy}$ in the first layer, which stems from inconsistencies between design and fabrication. Additionally, the disparity between diagonal and off-diagonal channels is closely associated with energy differences: the transmitted energy of channels J_{xx} and J_{yy} ($\int\int |a_1(x, y)|^2 dxdy$) is 1.87 times greater than that of channels J_{xy} and J_{yx} ($\int\int |a_2(x, y)|^2 dxdy$). With the higher energy conversion efficiency, channels J_{xx} and J_{yy} possess higher SNR, and this helps to maintain superior reconstructions despite the noise induced by displacements. To conclude, our scheme verifies a significant improvement in alignment tolerances of cascaded metasurfaces, providing a reference for the design of multi-layer metasurfaces with the need for cost-effective production. This robustness can also make the device more stable to external vibrations, ensuring a more durable and reliable operation toward integration.

Furthermore, the significant axial displacement tolerance of the cascaded metasurface enables the experimental demonstration of specific functions in the backward transmission direction, with the interlayer spacing consistently maintained at 100 μm (Figure 4c). The backward transmitted Jones matrix $J^b(x, y)$ adheres to the following rules: $J^b_{xx}(x, y) = J_{xx}(-x, y)$, $J^b_{xy}(x, y) = J_{yx}(-x, y)$, $J^b_{yx}(x, y) = J_{xy}(-x, y)$, and $J^b_{yy}(x, y) = J_{yy}(-x, y)$, which can be derived from the reciprocity principle. As the spatial light modulations are collectively flipped along the y-axes, the modulations of cross-polarization channels are subjected to additional swaps based on the reciprocal law. Consequently, it is possible to design more intriguing vectorial light field modulators that can be operated bidirectionally and possess misalignment robustness based on our method. Comparatively, it is nearly unattainable by using phase-cascaded metasurfaces with a predetermined distance. (More details are provided in Section S7, Supporting Information).

For comparison, we design a phase-cascaded metasurface without spatial frequency optimization, which exhibits stringent requirements for alignment and fabrication precision. The first layer's diagonal and off-diagonal channels are further endowed with birefringent phase distributions that lack spatial frequency optimization, building on the previous polarization encryption. In this case, each layer can independently encode different holograms via phase modulation. The reconstruction of holographic images of the cascaded metasurface depends on the precise matching of the two layers' modulation effects. (More details are provided in Section S8, Supporting Information).

For the convenience of conducting experiments, the macro pixel, size, and interlayer spacing of metasurfaces are respectively configured at 8 μm, 1 mm, and 50 μm. The corresponding SEM images of the first and second layers are provided in **Figure** 5a. The modulation effects of separable and cascaded metasurfaces are measured individually. As observed, the first layer displays a polarization encrypted QR code and projects holographic numbers "1" and "2" in the far field simultaneously. The second layer reconstructs holographic numbers "3" and "4" in the far field. After cascading them with a designed spacing of 50 μm, holographic letters "A", "B", "C", and "D" located in the far field appear in the cascaded channels J_{xx}, J_{xy}, J_{yx}, and J_{yy}, respectively. However, the reconstructed results

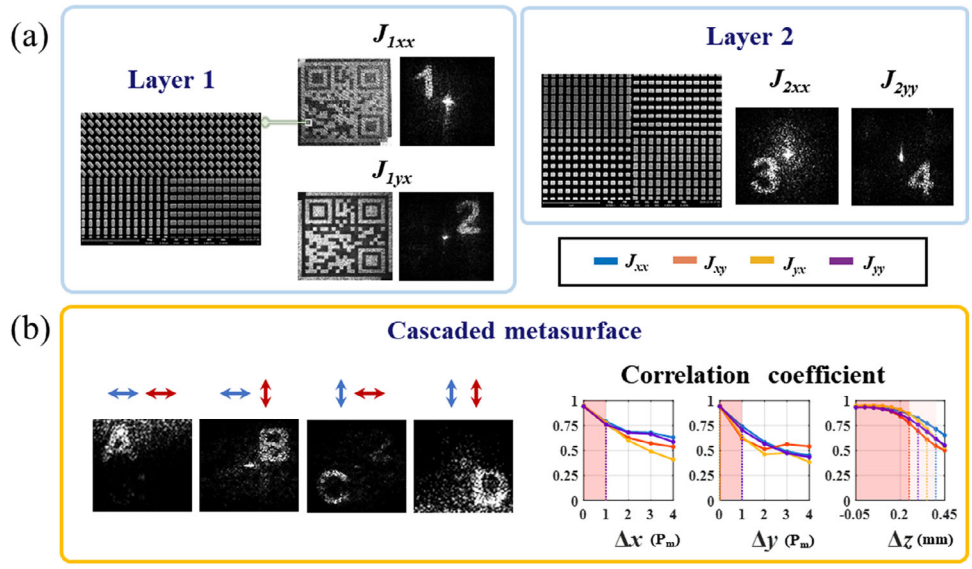

Figure 5. Design and experimental validation of the control group. a) SEM images and experimental results of Layer 1 and Layer 2. Both near-field polarization encryption and far-field holography are successfully demonstrated for Layer 1, and birefringent holography for Layer 2 is also illustrated. b) Experimentally captured images of the control group across Jones matrix channels, along with the misalignment assessment of the control group. The control group's misalignment assessment reveals a strict 1-pixel tolerance for lateral shifts and limited tolerance for axial displacements.

in Figure 5c exhibit a decline in quality and an increase in noise levels, indicating that the phase-cascaded scheme is more susceptible to fabrication imperfections. Therefore, additional vectorial multichannel modulations are less discernible due to the reduction of SNR. Subsequently, we calculate the correlation coefficients against diverse misalignments of this approach. The lateral displacement tolerance is confined to a mere 1 macro pixel, while the maximum axial misalignment that appears in J_{xx} the channel is ≈400 μm. The experimentally measured results, which showcase a notably low SNR, are consistent with the simulation outcomes of lateral displacements. When the lateral displacements exceed 1 macro pixel, the holographic letters are completely obscured in the noise. However, the measured results could only be distinguishable for the axial misalignment within ±50 μm, which is much lower than the simulation results (More details are provided in the S8, Supporting Information).

4. Conclusion

In this study, we first summarize and demonstrate the generalized polarization manipulation principles according to the analysis of polarization eigenstates and dichroism, retardance, and common phase inherent to such devices. Subsequently, we demonstrate the superior polarization manipulation capabilities of bilayer metasurfaces based on the modeling of cascaded units. The mathematical and computational explorations confirm the feasibility of arbitrary polarization eigenstate and phase control, with the Jones matrix capable of adopting any unitary matrix form. Continuing our study, we explore the design scheme of pixel-wise cascaded metasurfaces for multichannel vectorial multiplexing. Four independent and nine distinct holographic modulations are successfully realized across the multiplexed channels of cascaded metasurfaces, providing advanced solutions for high-capacity and versatile wavefront manipulations, which can adapt to applications in optical display, communication, storage, and beyond.

Furthermore, by employing spatial frequency optimization, the framework's robustness to 3D misalignment is notably enhanced. Our study verifies that the key to enhancing the misalignment robustness of multilayer metasurfaces is to minimize the distortion of interlayer wavefront transmission as much as possible. The distortion of interlayer wavefront transmission, which is indicated by the induced phase $\varphi(f_x,f_y)$ in the spatial frequency domain, can be alleviated by optimizing the bandwidth of $\varphi(f_x,f_y)$. The optimized design exhibits maximum measured lateral and axial displacement tolerances that are, respectively, 20-fold and 18-fold superior to those of the control group. Contrary to the cascaded metasurfaces designed for precision sensing and detection,[20c–f] our work provides a solution for low-precision and high-stability assembly processes, enabling the transition of assembly tolerances from the nanometer to the micrometer scale. This reduction relaxes the requirement for high-precision translation stages and laser measurement devices, ensuring the feasibility of cost-effective mass production. Moreover, by predesigning the energy conversion efficiencies of various polarization channels, the misalignment tolerances of these channels can be different, which can be utilized to develop a multi-step alignment technique. The greater tolerances ensure a coarse alignment for rapid initial positioning, while the narrower tolerances can be applied for further fine alignment.

Additionally, extra polarization manipulation approaches and potential alignment applications can be developed. Considering that two or more unitary matrices can be combined together to generate a complex matrix, by integrating two or multiple cascaded units into one synthetic unit, the optical response in the form of arbitrary complex-amplitude Jones matrix can be designed, providing convenient approaches for vectorial wavefronts shaping. Given the extensive application potential of multi-layer

metasurfaces in optical diffraction neural networks,[4a,5b,20b] nonreciprocal optical isolators,[18] full-space light manipulation,[24] we believe our work will spur innovative design approaches and meaningful advancements in the field.

Supporting Information

Supporting Information is available from the Wiley Online Library or from the author.

Acknowledgements

National Key Research and Development Program of China (2021YFA1401200); National Natural Science Foundation of China (No. U21A20140) and Beijing Natural Science Foundation (JQ24028).

Conflict of Interest

The authors declare no conflict of interest.

Data Availability Statement

The data that support the findings of this study are available from the corresponding author upon reasonable request.

Keywords

cascaded metasurfaces, misalignment robustness, polarization eigenstates and dichroism, vectorial wavefront manipulations

Received: February 10, 2025
Revised: April 22, 2025
Published online: May 12, 2025

[1] a) L. Huang, X. Chen, H. Mühlenbernd, H. Zhang, S. Chen, B. Bai, Q. Tan, G. Jin, K.-W. Cheah, C.-W. Qiu, J. Li, T. Zentgraf, S. Zhang, *Nat. Commun.* **2013**, *4*, 2808; b) S. So, J. Kim, T. Badloe, C. Lee, Y. Yang, H. Kang, J. Rho, *Adv. Mater.* **2023**, *35*, 2208520; c) N. A. Rubin, A. Zaidi, A. H. Dorrah, Z. Shi, F. Capasso, *Sci. Adv.* **2021**, *7*, abg7488; d) H. Ren, X. Fang, J. Jang, J. Bürger, J. Rho, S. A. Maier, *Nat. Nanotechnol.* **2020**, *15*, 948; e) X. Li, Q. Chen, X. Zhang, R. Zhao, S. Xiao, Y. Wang, L. Huang, *Opto-Electron. Adv.* **2023**, *6*, 220060.

[2] a) C. Liaskos, S. Nie, A. Tsioliaridou, A. Pitsillides, S. Ioannidis, I. Akyildiz, in *IEEE Communications Magazine*, IEEE, New York, USA **2018**, pp. 162–169; b) L. Li, H. Zhao, C. Liu, L. Li, T. J. Cui, *eLight* **2022**, *2*, 7; c) N. Shlezinger, G. C. Alexandropoulos, M. F. Imani, Y. C. Eldar, D. R. Smith, in *IEEE Wireless Communications*, IEEE, New York, USA **2021**, pp. 106–113; d) J. Tao, Q. You, Z. Li, M. Luo, Z. Liu, Y. Qiu, Y. Yang, Y. Zeng, Z. He, X. Xiao, *Adv. Mater.* **2022**, *34*, 2106080.

[3] a) H. Kwon, E. Arbabi, S. M. Kamali, M. Faraji-Dana, A. Faraon, *Nat. Photonics* **2020**, *14*, 109; b) R. J. Martins, E. Marinov, M. Aziz Ben Youssef, C. Kyrou, M. Joubert, C. Colmagro, V. Gâté, C. Turbil, P.-M. Coulon, D. Turover, S. Khadir, M. Giudici, C. Klitis, M. Sorel, P. Genevet, *Nat. Commun.* **2022**, *13*, 5724; c) J. Zhou, S. Liu, H. Qian, Y. Li, H. Luo, S. Wen, Z. Zhou, G. Guo, B. Shi, Z. Liu, *Sci. Adv.* **2020**, *6*, abc4385; d) A. Zaidi, N. A. Rubin, M. L. Meretska, L. W. Li, A. H. Dorrah, J.-S. Park, F. Capasso, *Nat. Photonics* **2024**, *18*, 704.

[4] a) E. Tseng, S. Colburn, J. Whitehead, L. Huang, S.-H. Baek, A. Majumdar, F. Heide, *Nat. Commun.* **2021**, *12*, 6493; b) X. Zou, G. Zheng, Q. Yuan, W. Zang, R. Chen, T. Li, L. Li, S. Wang, Z. Wang, S. Zhu, *Photonix* **2020**, *1*, 2; c) F. Guan, X. Guo, K. Zeng, S. Zhang, Z. Nie, S. Ma, Q. Dai, J. Pendry, X. Zhang, S. Zhang, *Science* **2023**, *381*, 766.

[5] a) J. Hu, D. Mengu, D. C. Tzarouchis, B. Edwards, N. Engheta, A. Ozcan, *Nat. Commun.* **2024**, *15*, 1525; b) M. S. Sakib Rahman, A. Ozcan, *ACS Photonics* **2024**, *11*, 2906; c) D. Mengu, Y. Zhao, N. T. Yardimci, Y. Rivenson, M. Jarrahi, A. Ozcan, *Nanophotonics* **2020**, *9*, 4207.

[6] Z. Lin, L. Huang, Z. T. Xu, X. Li, T. Zentgraf, Y. Wang, *Nanophotonics* **2019**, *7*, 1900782.

[7] N. A. Rubin, G. D'Aversa, P. Chevalier, Z. Shi, W. T. Chen, F. Capasso, *Science* **2019**, *365*, aax1839.

[8] a) S. Divitt, W. Zhu, C. Zhang, H. J. Lezec, A. Agrawal, *Science* **2019**, *364*, 890; b) H. He, Y. Zhang, Y. Shao, Y. Zhang, G. Geng, J. Li, X. Li, Y. Wang, L. Bian, J. Zhang, L. Huang, *Adv. Mater.* **2024**, *36*, 2313357.

[9] a) H. Sroor, Y.-W. Huang, B. Sephton, D. Naidoo, A. Vallés, V. Ginis, C.-W. Qiu, A. Ambrosio, F. Capasso, A. Forbes, *Nat. Photonics* **2020**, *14*, 498; b) X. Zhang, L. Huang, R. Zhao, H. Zhou, X. Li, G. Geng, J. Li, X. Li, Y. Wang, S. Zhang, *Sci. Adv.* **2022**, *8*, abp8073.

[10] a) A. Arbabi, Y. Horie, M. Bagheri, A. Faraon, *Nat. Nanotechnol.* **2015**, *10*, 937; b) C. Menzel, C. Rockstuhl, F. Lederer, *Phys. Rev. A* **2010**, *82*, 053811; c) Z. Shi, N. A. Rubin, J.-S. Park, F. Capasso, *Phys. Rev. Lett.* **2022**, *129*, 167403.

[11] a) S. Wang, S. Wen, Z.-L. Deng, X. Li, Y. Yang, *Phys. Rev. Lett.* **2023**, *130*, 123801; b) S. Wang, Z.-L. Deng, Y. Wang, Q. Zhou, X. Wang, Y. Cao, B.-O. Guan, S. Xiao, X. Li, *Light: Sci. Appl.* **2021**, *10*, 24.

[12] J. B. Mueller, N. A. Rubin, R. C. Devlin, B. Groever, F. Capasso, *Phys. Rev. Lett.* **2017**, *118*, 113901.

[13] M. Liu, W. Zhu, P. Huo, L. Feng, M. Song, C. Zhang, L. Chen, H. J. Lezec, Y. Lu, A. Agrawal, T. Xu, *Light-Sci. Appl.* **2021**, *10*, 107.

[14] a) Z. H. Jiang, L. Kang, T. Yue, H. X. Xu, Y. Yang, Z. Jin, C. Yu, W. Hong, D. H. Werner, C. W. Qiu, *Adv. Mater.* **2020**, *32*, 1903983; b) Y. Bao, J. Ni, C. W. Qiu, *Adv. Mater.* **2020**, *32*, 1905659.

[15] a) B. Xiong, Y. Liu, Y. Xu, L. Deng, C.-W. Chen, J.-N. Wang, R. Peng, Y. Lai, Y. Liu, M. Wang, *Science* **2023**, *379*, 294; b) I. Kim, J. Jang, G. Kim, J. Lee, T. Badloe, J. Mun, J. Rho, *Nat. Commun.* **2021**, *12*, 3614; c) F. Ding, B. Chang, Q. Wei, L. Huang, X. Guan, S. I. Bozhevolnyi, *Laser Photonics Rev.* **2020**, *14*, 2000116; d) R. Zhao, B. Sain, Q. Wei, C. Tang, X. Li, T. Weiss, L. Huang, Y. Wang, T. Zentgraf, *Light-Sci. Appl.* **2018**, *7*, 95; e) Z. L. Deng, M. Jin, X. Ye, S. Wang, T. Shi, J. Deng, N. Mao, Y. Cao, B. O. Guan, A. Alù, *Adv. Funct. Mater.* **2020**, *30*, 1910610; f) Z.-L. Deng, J. Deng, X. Zhuang, S. Wang, K. Li, Y. Wang, Y. Chi, X. Ye, J. Xu, G. P. Wang, R. Zhao, X. Wang, Y. Cao, X. Cheng, G. Li, X. Li, *Nano Lett.* **2018**, *18*, 2885; g) S. Zhang, L. Huang, X. Li, R. Zhao, Q. Wei, H. Zhou, Q. Jiang, G. Geng, J. Li, X. Li, Y. Wang, *ACS Photonics* **2021**, *8*, 1746.

[16] a) L.-J. Kong, W. Zhang, P. Li, X. Guo, J. Zhang, F. Zhang, J. Zhao, X. Zhang, *Nat. Commun.* **2022**, *13*, 2705; b) R. Wang, Y. Intaravanne, S. Li, J. Han, S. Chen, J. Liu, S. Zhang, L. Li, X. Chen, *Nano Lett.* **2021**, *21*, 2081.

[17] a) T. Shi, Z.-L. Deng, G. Geng, X. Zeng, Y. Zeng, G. Hu, A. Overvig, J. Li, C.-W. Qiu, A. Alù, Y. S. Kivshar, X. Li, *Nat. Commun.* **2022**, *13*, 4111; b) A. Overvig, N. Yu, A. Alù, *Phys. Rev. Lett.* **2021**, *126*, 073001; c) W. Liu, B. Wang, Y. Zhang, J. Wang, M. Zhao, F. Guan, X. Liu, L. Shi, J. Zi, *Phys. Rev. Lett.* **2019**, *123*, 116104; d) T. Chang, J. Jung, S. H. Nam, H. Kim, J. U. Kim, N. Kim, S. Jeon, M. Heo, J. Shin, *Adv. Mater.* **2022**, *34*, 2204085; e) Y. Bao, F. Nan, J. Yan, X. Yang, C.-W. Qiu, B. Li, *Nat. Commun.* **2022**, *13*, 7550; f) Y. Yuan, K. Zhang, Q. Wu, S. N. Burokur, P. Genevet, *Nat. Commun.* **2024**, *15*, 6682; g) H. Li, A. Yu, C. Pang, Y. Wang, J. Qi, *Laser Photonics Rev.* **2024**, *18*, 2400300.

[18] D. Frese, Q. Wei, Y. Wang, L. Huang, T. Zentgraf, *Nano Lett.* **2019**, *19*, 3976.

[19] Y. Zhou, I. I. Kravchenko, H. Wang, H. Zheng, G. Gu, J. Valentine, *Light-Sci. Appl.* **2019**, *8*, 80.
[20] a) Y. Luo, C. H. Chu, S. Vyas, H. Y. Kuo, Y. H. Chia, M. K. Chen, X. Shi, T. Tanaka, H. Misawa, Y.-Y. Huang, D. P. Tsai, *Nano Lett.* **2021**, *21*, 5133; b) C. He, D. Zhao, F. Fan, H. Zhou, X. Li, Y. Li, J. Li, F. Dong, Y.-X. Miao, Y. Wang, L. Huang, *Opto-Electron. Adv.* **2024**, *7*, 230005; c) H. Zhou, X. Li, H. Wang, S. Zhang, Z. Su, Q. Jiang, N. Ullah, X. Li, Y. Wang, L. Huang, *Opt. Express* **2022**, *30*, 24285; d) X. Zhang, T. Li, H. Zhou, Y. Li, J. Li, X. Li, Y. Wang, L. Huang, *Laser Photonics Rev.* **2024**, *18*, 2300887; e) Q. Wei, L. Huang, R. Zhao, G. Geng, J. Li, X. Li, Y. Wang, *Adv. Opt. Mater.* **2022**, *10*, 2102166; f) P. Georgi, Q. Wei, B. Sain, C. Schlickriede, Y. Wang, L. Huang, T. Zentgraf, *Sci. Adv.* **2021**, *7*, abf9718.
[21] a) N. A. Rubin, Z. Shi, F. Capasso, *Adv. Opt. Photonics* **2022**, *13*, 836; b) J. N. Damask, *Polarization Optics in Telecommunications*, Springer Science & Business Media, Heidelberg, Germany **2004**.
[22] Q. Wei, L. Huang, X. Li, J. Liu, Y. Wang, *Adv. Opt. Mater.* **2017**, *5*, 1700434.
[23] X. Zhang, X. Li, S. Zhang, R. Zhao, Y. Wang, C. Chen, Y. Wang, L. Huang, *Laser Photonics Rev.* **2024**, *18*, 2400539.
[24] L. Deng, Z. Li, Z. Zhou, Z. He, Y. Zeng, G. Zheng, S. Yu, *Adv. Opt. Mater.* **2022**, *10*, 2102179.